Available online at www.sciencedirect.com
SCIENCE DIRECT®
Acta Materialia 52 (2004) 1535–1542
Acta MATERIALIA
www.actamat-journals.com

Dislocation motion in thin Cu foils: a comparison between computer simulations and experiment

Zhiqiang Wang [a,*], Rodney J. McCabe [b], Nasr M. Ghoniem [a], Richard LeSar [c], Amit Misra [b], Terence E. Mitchell [b]

[a] Department of Mechanical and Aerospace Engineering, University of California, 420 Westwood Plaza, Los Angeles, CA 90095-1597, USA
[b] Materials Science and Technology Division, MS G755, Los Alamos National Laboratory, Los Alamos, NM 87545, USA
[c] Theoretical Division, T-12, MS B268, Los Alamos National Laboratory, Los Alamos, NM 87545, USA

Received 23 July 2003; received in revised form 4 December 2003; accepted 5 December 2003

Abstract

Discrete dislocation dynamics (DD) simulations in conjunction with stereo and in situ straining transmission electronic microscopy (TEM) were used to study dislocation motion in thin Cu foils. Stereo imaging prior to and following in situ tensile straining is utilized to describe the three-dimensional (3D) evolution of dislocation structures with incremental straining and observation by TEM. The initial 3D configuration is used as input for 3D discrete dislocation dynamics simulations, and the final 3D configuration serves to refine and validate the DD simulation, thereby providing a direct quantitative link between experiment and dislocation dynamics modeling. In the present experiment, we observed complex 3D structures of dislocations, with significant out-of-plane motion. Computer simulations incorporating the Friedel–Escaig cross-slip mechanism indicate that surface image forces are sufficiently strong to activate out-of-plane motion for screw dislocation segments near the surface. Cross-slip of screw segments and dislocation climb of edge components are shown to be necessary mechanisms for explaining the observed 3D dislocation motion.

Keywords: Discrete dislocation dynamics; Transmission electron microscopy; Copper; Dislocation motion; Cross-slip; Surface image force

1. Introduction

Computer simulations of the mechanical deformation of materials based on discrete dislocations are becoming a powerful tool for interrogation of various fundamental mechanisms that control the macroscopic aspects of material plasticity. In dislocation dynamics (DD) methods, forces on individual dislocations are calculated and the motion of the dislocations computed [1–7]. Nevertheless, accurate description of complex three-dimensional (3D) motion (e.g., glide, cross-slip, and climb) of dislocations requires direct experimental observation for validation of computer simulations. The lack of detailed experiments on the 3D motion of single dislocations does not allow computer simulations direct access to experimentally verifiable mechanisms that control dislocation configurations. Most dislocation microstructures in strained materials are highly complex, spanning many scales from the microscopic level to the polycrystalline domain. Therefore, comparison of computer simulation to such experiments can only be based on qualitative features of the microstructures.

Transmission electron microscopy (TEM) offers the most direct method of comparison for DD simulations. However, few such comparisons have been made to date, and these have been qualitative examinations and not quantitative comparisons between experiment and modeling [8,9,12]. Comparisons of DD simulations to static TEM images are necessarily indirect and qualitative since standard TEM images are 2D thin foil projections of static microstructures. Dynamic dislocation behavior in thin foils can be observed by in situ TEM,

* Corresponding author. Tel.: +1-310-825-8917; fax: +1-310-206-4830.
E-mail address: zhiqiang@seas.ucla.edu (Z. Wang).

1359-6454/$30.00 © 2003 Acta Materialia Inc. Published by Elsevier Ltd. All rights reserved.
doi:10.1016/j.actamat.2003.12.005

and several interesting experimental studies have been made using this technique [10,11]. Some 3D information about dislocation motion can be ascertained if traveling dislocations leave a slip trace on the surface. However, information on the relative positions of dislocations is largely limited to 2D results, and without 3D information on dislocation configurations, the elastic interactions between dislocations cannot be accurately determined. A technique has been developed in which 3D dislocation configurations can be quantified before and during an in situ straining TEM experiment [13]. Although direct 3D observations of dislocation motion is not possible, knowledge of 3D configurations preceding and following deformation, along with 2D in situ records of motion, can be used to reconstruct the overall 3D behavior. Such information can also be used for direct validation of 3D DD simulations.

The present study details a direct comparison between experimental observations and computer simulations of dislocations in thin foils. The goal is to use these comparisons to ascertain the nature of forces on dislocations and the salient mechanisms that control their motion. The effects of the constrained geometry of the foil and the free surface on dislocation motion are explored. Simplified elasticity calculations of dislocation forces and motion are not reliable to correlate with experimental data because of the complex 3D structure of observed dislocations and the influence of surface image forces. Thus, utilization of 3D computer simulations, including surface image effects, is necessary.

We specifically examine here two effects that are particular to dislocation behavior in thin foils. First, since dislocation loops may terminate at free surfaces, computer simulations must track the position of dislocation-free surface intersections. Thus, special boundary conditions must be applied to the study of thin foil deformation. Second, the free surfaces of a thin foil may strongly influence dislocation behavior by introducing image stresses, which become significant when dislocations approach the surface. Strong image forces can influence dislocations by enhancing their out-of-plane motion through cross-slip and climb mechanisms.

Numerous experiments have shown that cross-slip, which is thermally activated, plays an important role during stage-III work hardening in FCC single crystals [15–17]. Double cross-slip results in dislocation generation by expanding new Frank–Read sources on neighboring glide planes [18]. Only segments of screw (or nearly screw) character may perform cross-slip, because they are able to move on any favorably oriented glide plane. The probability of a dislocation segment to cross-slip onto a neighboring slip plane increases significantly when the resolved shear stress on that plane is high. Any large internal stress field, which may arise from inclusions and other obstacles to glide, surfaces, or interfaces, may induce cross-slip events.

Motion out of the glide plane can also be accomplished by climb [25–27]. At low temperatures or in the absence of a non-equilibrium concentration of point defects, dislocation motion is restricted almost entirely to glide. However, at higher temperatures or owing to a locally high stress, an edge dislocation can move out of its slip plane by climb.

The objective of this work is to utilize 3D stereo-TEM in conjunction with in situ straining TEM to describe the evolution of the spatial topology of dislocations in thin foils. DD computer simulations are used to investigate the salient mechanisms that determine experimentally observed dislocation shapes. In doing so, we explore the importance of image surface forces and their effects on out-of-plane dislocation motion by the cross-slip and climb mechanisms. We show that surface-force induced cross-slip greatly influences the structure and dynamics of the dislocation microstructure in thin foils, and that dislocation motion in thin foils may not be representative of bulk behavior. To our knowledge, this is the first direct comparison of experiment and simulation of moving dislocations.

2. Experimental procedure and results

Stereo-TEM was used in conjunction with in situ straining to describe the evolution of the spatial distribution of dislocations in thin Cu foils. In situ TEM experiments are generally used to develop an understanding of bulk material properties. However, the inference of bulk material properties from thin foil in situ observations is often controversial due to the effects of free surfaces on dislocation configurations. We plan here to link direct experimental observations of dislocation motion and reconfiguration with computer simulations so as to discern dislocation mechanisms that are specific to thin films. Examining thin foil behavior is an advantage in that it includes surface effects, and can thus better gauge the fidelity of DD models.

TEM in situ tensile specimens were cut, ground, and electro-polished from a well-annealed copper sample. Tensile Cu foils were prepared with dimensions of 11.5 mm by 2.5 mm and a thickness of approximately 175 μm as shown in Fig. 1. Electrolytic polishing was used to

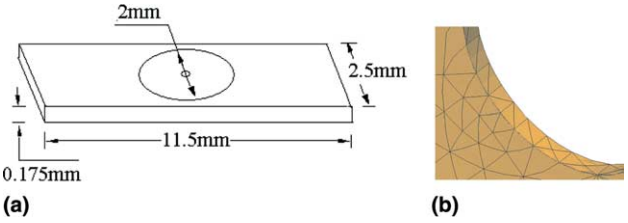

Fig. 1. (a) The solid model of the sample and (b) FEM mesh around the central hole.

thin the center of the specimen to perforation. The geometry of the thinned region can be approximated as two hemispherical dimples intersecting the top and bottom surfaces at 2-mm circles. Thinning produced a hole approximately 400 μm in diameter, and the specimen thickness at the edge of the hole is generally 10–20 nm. The experimental observations were made near the top edge of the hole at a position where the sample thickness is about 200 nm.

Deformation was carried out inside the TEM using a displacement control, single tilt, straining specimen holder. During in situ straining, TEM experiments, it is advantageous to pre-strain the specimen while viewing an area of interest until some dislocation activity begins. This is primarily to ensure that dislocation motion will occur in the area of interest before spending significant time doing stereo and Burgers vector analysis. However, once the specimen is pre-strained, there is potential for the specimen to relax somewhat while analysis is being performed, and some dislocations can change position or escape the region being observed.

The stereo-coupled in situ experiments involve obtaining a 3D description of the dislocation configuration prior to and following in situ straining in the microscope. Three-dimensional configurations are obtained using a modified stereo-TEM technique detailed elsewhere [13]. Standard stereo-microscopy of crystalline materials is almost never possible with a single-tilt TEM holder making it unfeasible for all commercially available in situ straining TEM holders. The modified approach is a weak beam technique involving changing the sign of **g** (the imaging beam) and/or s_g (how far the imaging beam deviates from the exact Bragg condition) between images while tilting across a Kikuchi band that is at less than approximately 10° to the tilting direction.

The stereo pair and diffraction pattern demonstrating the modified stereo technique for the initial dislocation configuration is shown in Fig. 2, with the tensile axis direction vertical (same as stereo tilt axis and specimen holder axis). The positions of the dislocations are measured using a computer program that allows the user to mark points along a dislocation line with a 3D cursor while viewing micrographs stereoscopically [14]. The orientations of the tensile axis and specimen plane normal with respect to the grain are $[53\,(\bar{6}\bar{8})\,51]$ and $[(\bar{7}\bar{8})\,(\bar{1}\bar{5})\,61)]$, respectively. Based on this geometry, Schmid factors for the common fcc slip systems obtained assuming a simple tension assumption are given in Table 1. Burgers vector analysis was performed on several key dislocations. Dislocations labeled 11, 13, and 22 in Fig. 2 have a Burgers vector of $[1\,0\,1]$ and dislocation 12 has a Burgers vector of $[\bar{1}\,0\,\bar{1}]$.

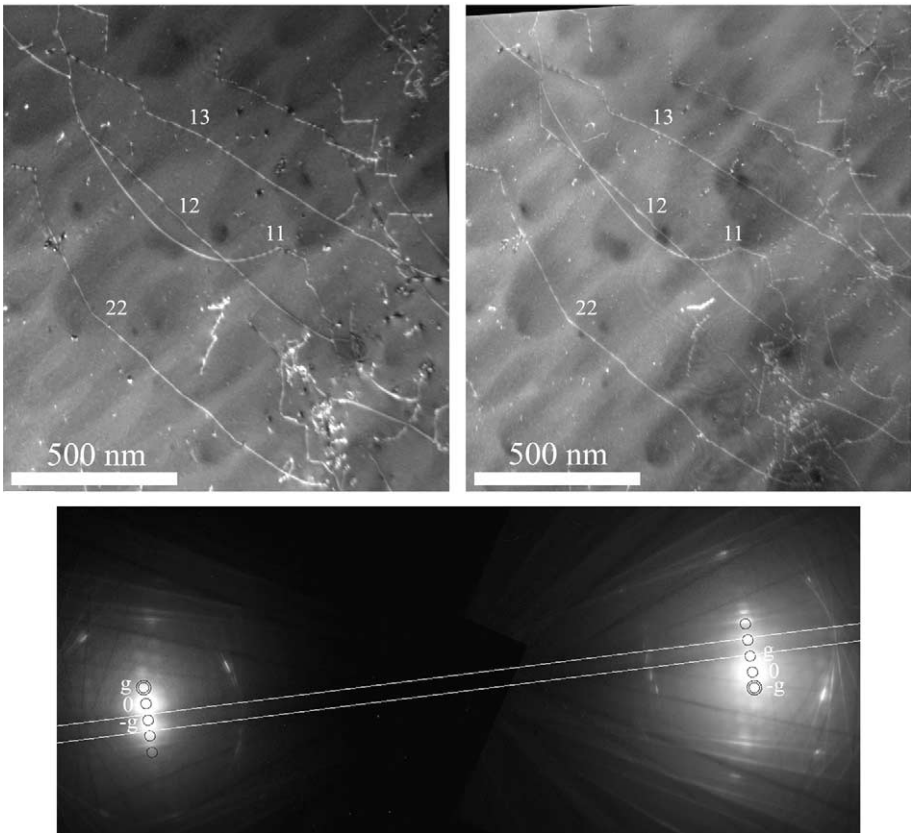

Fig. 2. Stereo pair (top) and diffraction pattern demonstrating the modified stereo technique.

Table 1
Schmid factors for the Cu thin foil under simple tension

$(1\,1\,1)$			$(1\,1\,\bar{1})$		
$[0\,1\,\bar{1}]$	$[1\,0\,\bar{1}]$	$[1\,\bar{1}\,0]$	$[0\,1\,1]$	$[1\,0\,1]$	$[1\,\bar{1}\,0]$
0.174	0.003	0.177	0.046	0.279	0.325
$(\bar{1}\,1\,1)$			$(1\,\bar{1}\,1)$		
$[0\,1\,\bar{1}]$	$[1\,0\,1]$	$[1\,1\,0]$	$[0\,1\,1]$	$[1\,0\,\bar{1}]$	$[1\,1\,0]$
0.339	0.296	0.043	0.119	0.014	0.105

During in situ straining, dislocation motion was monitored in the TEM at 30 frames/s. Fig. 3 shows dislocation configurations at various times during the in situ straining. Comparing the first frame of Fig. 3 with the configuration seen in Fig. 2, it is evident that dislocation 11 and 22 moved between the time when the stereo pair was taken and when the straining was continued and recorded. However, these two dislocations do not move during further straining. Three-dimensional representations of the dislocation configuration before and after straining are given in Fig. 4. In the 3D

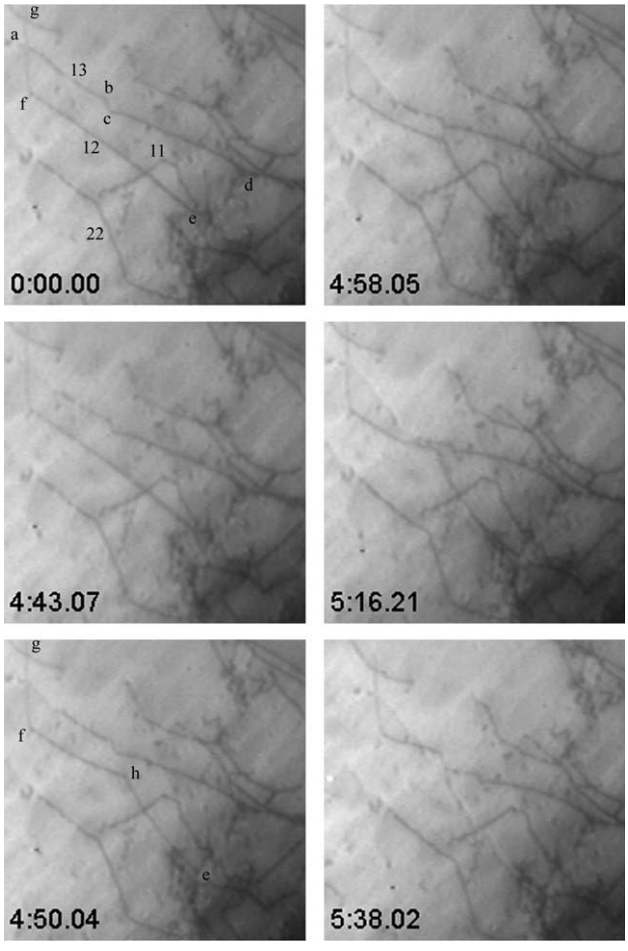

Fig. 3. Time sequence of in situ TEM measurements during straining. Time units are min:s:s fraction.

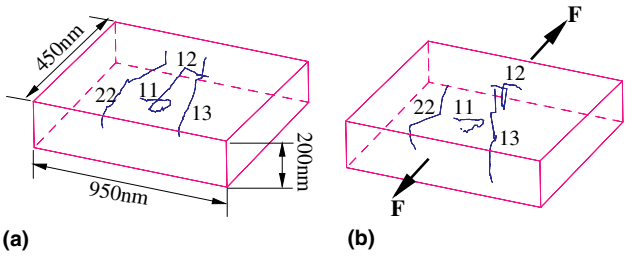

Fig. 4. Three-dimensional rendering of experimentally observed dislocation configurations in the Cu thin foil: (a) before deformation and (b) after deformation.

representations and the DD calculations based on these configurations, the initial and final configurations of dislocation 11 are assumed to be the same, specifically the configuration given by the final stereo pair. This assumption is reasonable, since dislocations 11 and 22 do not react with one another in changing configuration, because the two dislocations have the same Burgers vector.

Dislocations 12 and 13 share the same primary glide plane, $(1\,1\,\bar{1})$, and Burgers vector but have opposite signs. Hence, they move in opposite directions. One end of dislocation 13 is pinned at a node (point labeled (d) in the first frame), while the other end terminates at the foil surface (point labeled (a) in first frame). There is a jog, labeled (bc), along the length of dislocation 13 lying on the $(\bar{1}\,1\,1)$ plane. During straining, the right end remains pinned at the node and the segment (ab) glides downward in the image. Dislocation 12 starts out pinned at a different node, labeled (e). A straight segment (labeled (ef)) of dislocation 12 extends from the node diagonally across the image towards the top left corner where it jogs upwards towards the free surface (segment labeled (fg)). During straining, unlike dislocation 13, dislocation 12 escapes from the pinning point (e) (third frame) first, only to be pinned again at another node directly below the first pinning point, labeled (e) in the third frame. The result is the formation of a jog along the length of dislocation 12 as seen in frame 3. The segment (he) appears to glide to the left, while insignificant movement of segment (hfg) was discerned up to frame 3. In frames 4–6, the segment (fh) glides upward in the image. This motion eventually leads to dislocation 12 escaping from the pinning point (e) and soon after that, a large portion of the dislocation segment (he) escapes to the surface. A key question not resolved from Fig. 3 is whether dislocations 12 and 13 intersect during glide (frames 4 and 5 appear to indicate a possible interaction). This is very difficult to discern from the 2D in situ straining images, but the stereo imaging (Fig. 3) reveals that these dislocations do not intersect. Another question is the distance of the various dislocation segments from the free surfaces that can only be resolved from stereo imaging of the in situ strained dislocation substructures. As shown

later in this paper, having quantitative information of the dislocation positions in the in situ straining experiment is crucial in modeling the dynamics of dislocations in thin foils.

The bowed out segment of dislocation 11 in Fig. 4 is not visible in the first frame of Fig. 3. This implies that this segment glided out to the free surface in the time between stereo imaging and the onset of further straining. Since the specimen is under strain during this time, beam heating may lead to escape of bowed out segments that are near the free surface. The remaining segments seen in Fig. 3 are not on the glide plane, and hence no further motion is detected.

Dislocation 22 appears as a straight line in Fig. 2 but kinked in the first frame of Fig. 3. It is possible that it experiences a similar type of motion to that described above for dislocation 12 in frames 1–3. The kinked dislocation 22 may be strongly pinned at both ends (although the details of the pinning points are not discerned clearly in these images) and hence, no further motion is detected in the in situ straining sequence shown in Fig. 3. Motion of dislocations motions shown in Fig. 2 appear to be more evident for dislocations that terminate at a free surface. The influence of surface forces on dislocation dynamics in thin films is discussed in more detail in the DD simulation section of this paper.

Based on slip trace analysis, dislocation glide has taken place on two glide planes: $(1\,1\,\bar{1})$ and $(\bar{1}\,1\,1)$. The resolved shear stresses for the $[1\,0\,1](1\,1\,\bar{1})$ and $[1\,0\,1](\bar{1}\,1\,1)$ dislocations are approximately the same, although slightly less than the highest stressed slip systems.

There is extensive discussion of the error involved in conventional and modified stereo-TEM given elsewhere [13]. The experimental error in the third dimension (z) for standard stereo-TEM depends on the stereo angle and is around an order of magnitude greater than the measurement error in the other two dimensions. With the measurement error in the x and y directions being on the order of 1 nm, the measurement error in the z-direction is around 10 nm. The error for the modified technique is the same as for standard stereo provided both $\mathbf{g}$ and s_g change sign but not magnitude [13]. In the present case, these ideal imaging conditions were not obtained, likely resulting in a somewhat larger error in z. These errors are to be kept in mind during the direct comparison of the modeling results to the experimental data.

3. Dislocation dynamics in thin foils

In the present study, we use the parametric dislocation dynamics (PDD) method to simulate the motion and interaction of dislocations [5–7]. We incorporate here additional forces on dislocations as a result of their interaction with the free surface. There are several models available to calculate the effects of surface forces, or to directly include the image stress field into DD simulations. These approaches include Lothe's energy theorem [19], Gosling and Willis' Green's function method [20], and the superposition method based on solution of the Boussinesq problem [20]. For complex dislocation configurations and boundary conditions, image stresses due to surfaces and interfaces can now be computed by the finite element method (FEM) [23,24]. In this work, we implemented Lothe's theorem for direct calculations of surface forces into the PDD code [6]. For an isotropic medium, Lothe and co-workers [19] determined the force per unit length induced by a free surface on a straight dislocation segment [3]:

$$\mathbf{F}=\frac{\mu b^2}{4\pi(1-\nu)\lambda}\left[|(1-\nu\cos^2\beta)\tan\theta|\mathbf{n}_1+|2\nu\cos\beta\sin\beta|\mathbf{n}_2\right], \tag{1}$$

where μ, ν are the material's shear modulus and Poisson's ratio, respectively. Parameters are shown in Fig. 5. λ is the distance from point P, where the force is evaluated, to point O at which the dislocation line intersects the free surface. $\mathbf{n}_1$ is a unit vector on the plane OO'P, with direction perpendicular to the dislocation line, $\mathbf{n}_2$ is a unit vector on the plane containing OP and the Burgers vector, with direction perpendicular to the dislocation line on the glide plane. $\mathbf{n}_1$ represents the direction of the force component, which acts to rotate the dislocation line so that it is normal to the surface, while $\mathbf{n}_2$ represents the direction of the force component, which acts to align the dislocation along its Burgers vector. The angle β is between the tangent and Burgers vectors, while θ refers to the angle between the tangent vector and the surface normal. The surface force is then decomposed to a component on the glide plane, and added to be a part of the resolved glide forces, along with those dictated by the applied stress and interaction forces. Because curved dislocation segments are employed, the tangent vector is extended to its intersection

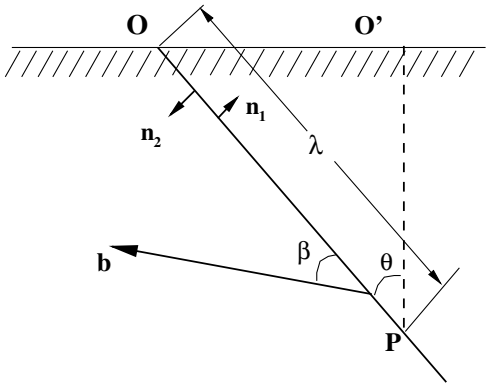

Fig. 5. Illustration of Lothe's formula to calculate surface image force.

with the free surface, and Eq. (1) is used to compute the force per unit length at any point on the dislocation line. This force is also integrated along the parametric curves to determine the nodal positions and coordinates, as described in [6].

In the present model, dislocation loops are discretized into several curved segments that can glide on different glide planes (see Table 2). Internal nodes belonging to two different glide planes can only move along the intersection line of the two planes. Dislocations may end at the surface or at some joint nodes with other dislocations inside the material. Surface nodes can move along the intersection line of the glide and surface planes. Since the motion of surface nodes is associated with the creation of surface steps, the mobility of these nodes is assumed to be 20% of the bulk mobility (10^4 Pa^{-1} s^{-1}) [7].

Because screw dislocation segments can move on different intersecting glide planes, cross-slip is possible [18]. In the present simulations, the orientation of various segments are checked to determine if the average tangent vector on the segment is aligned within 15° of its Burgers vector orientation. If that is the case, another check is made on the resolved shear stress magnitude on all glide planes on which the segment may glide. Following the Friedel–Escaig mechanism [15], the probability of a cross-slip event to occur is related to the activation energy and the resolved shear stress on any glide plane as [21,22]:

$$P = \beta \frac{L}{L_0} \frac{\delta t}{\delta t_0} \exp\left(V \frac{\tau - \tau_{III}}{kT}\right), \quad (2)$$

where β is a normalizing coefficient that makes the probability ranging from 0 to 1, $\tau_{III} = 32$ MPa is the critical resolved shear stress at the onset of stage III of work hardening, $V = 300b^3$ is the activation volume, k is the Boltzmann constant, T is the temperature, $L_0 = 1$ μm and $\delta t_0 = 1$ s are, respectively, references to length and time, τ is the resolved shear stress on the cross-slip plane, L is the length of the screw segment, and δt is the discrete time-step [22].

After the probabilities of cross-slip on each plane are calculated, the plane with a larger probability of cross-slip is selected for dislocation to move. When the dislocation segment approaches the free surface, the resolved shear stress on possible glide planes increases dramatically and the probability of cross-slip is enhanced. Further analysis of the experimental data also indicated the presence of many small jogs on dislocation lines. Such jogs can produce vacancies as they move towards the sample surface, which may result in additional out-of-plane motion due to climb of edge components as well. As a simple model of climb, comparison between the experimental and the computed dislocation structures was made and climb movement was attempted for segments that showed large differences. In summary, the simulations proceeded in the following way: (1) dislocation motion along glide planes only, (2) cross-slip motion, and (3) climb.

One uncertainty in the calculation is the stress state acting on experimentally observed dislocations. The direction of the shear stress was determined by examining the dislocation bow out and motion. In the simulations, the applied stress was increased until the final position of the dislocations matched the experiment. A 3D FEM was also used to analyze the stress state in the sample. The model consisted of 7880 tetrahedral elements, corresponding to 16,268 nodes. A displacement boundary condition was used, corresponding to sample straining by edge displacements in the range of (0–4) μm. A solid model for the sample is shown in Fig. 1. Results of the axial (normal) stress components along the tensile axis (y-direction) and along its perpendicular (x-direction) are shown in Fig. 6. Also shown in Fig. 7 is the corresponding normal stress contour around the central perforation. Although large stress gradients are observed near the central hole region, the zone where dislocations are observed extend over a relatively small

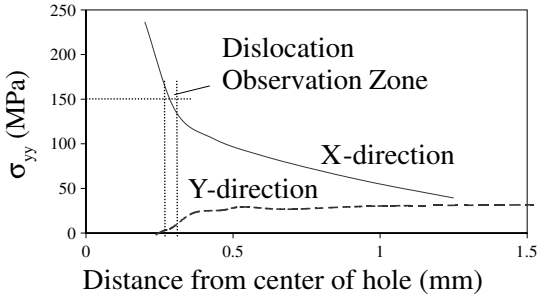

Fig. 6. FEM results for normal stress distribution in the sample along the axial direction (y) and its normal (x).

Table 2
Nodal segment distributions on dislocations, with corresponding Burgers vectors (**b**), glide plane Miller indices

Dislocation	Segment 1		Segment 2		Segment 3		b
	Miller	Nodes	Miller	Nodes	Miller	Nodes	
11	Jog	1–15	(1 1 $\bar{1}$)	15–16	($\bar{1}$ 1 1)	16–29	[1 0 1]
12	(1 1 $\bar{1}$)	1–7	($\bar{1}$ 1 1)	7–24	(1 1 $\bar{1}$)	24–41	[$\bar{1}$ 0 $\bar{1}$]
13	(1 1 $\bar{1}$)	1–27	($\bar{1}$ 1 1)	27–28	(1 1 $\bar{1}$)	28–36	[1 0 1]
22	(1 1 $\bar{1}$)	1–18	($\bar{1}$ 1 1)	18–37	(1 1 $\bar{1}$)	37–44	[1 0 1]

All segments are in mixed characters.

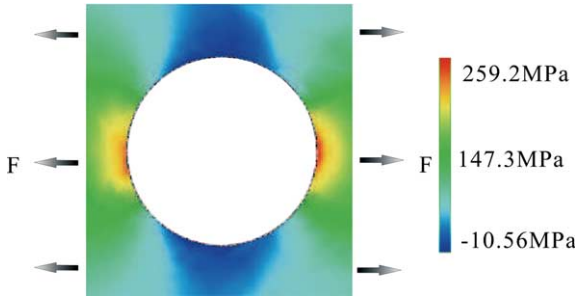

Fig. 7. FEM results for σ_{yy} contour around the central hole.

length (microns), and the axial stress level is estimated to be 150 MPa for the full 4 μm displacement. It is also found that the shear stress component in this zone is negligible, confirming that tensile stress state in our DD model is close to the correct value.

4. PDD simulations for experimental analysis

Initial PDD computer simulations of the experimental data restricted the motion of dislocations to movement on the glide plane. The initial results indicated that while the experimental dislocation motion on the glide planes is matched reasonably well in the simulations, motion in the direction normal to the TEM observation plane is greatly underestimated by the simulations. To be more concrete, with no climb or cross-slip mechanisms invoked, the difference between the simulations and experiments for dislocation 11 is approximately 16 nm within the observation plane and 12 nm out-of-plane, roughly within the experimental uncertainty. The other dislocations were less well determined, with a difference in dislocations 22 and 13 within the observation plane of approximately 61 nm and an out-of-plane error of 80 nm. The motion of dislocation 12 is even more poorly modeled, with an in-plane difference of 200 nm and an out-of-plane error of 140 nm.

PDD simulations that include dislocation cross-slip and climb (using the methods described above) were thus performed. These simulation results are shown in Fig. 8 and are compared with experimental observations of Figs. 2 and 4. The results show that dislocation 22 undergoes cross-slip motion, dislocation 13 climbs, and dislocation 12 shows both climb and cross-slip motion. Details of the cross-slip mechanism of dislocation 22 are shown in Fig. 9, where we see that the segment reconfigures from the original slip plane to the neighboring one with a higher probability of cross-slip motion. The cross-slip probabilities of two screw segments are listed in Table 3. It is obvious that cross-slip planes have larger probabilities. Although cross-slip does not have to happen on cross-slip plane, the dislocation segment will select the plane that has large a larger probability.

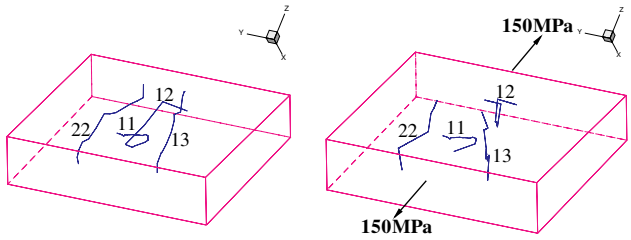

Fig. 8. Initial and final dislocation configurations simulated by PDD.

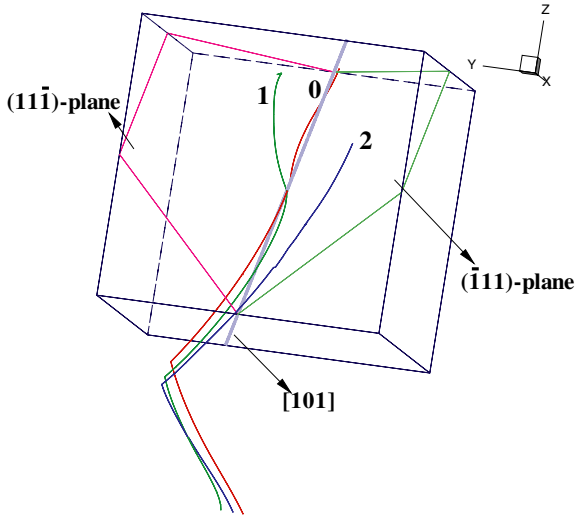

Fig. 9. Dislocation 22 positions during cross-slip motion: (1) final configuration without cross-slip and (2) final configuration with cross-slip.

Table 3
Probabilities of cross-slip of screw segments at an applied stresses of 100 MPa

Segment on dislocation	Original plane	Cross-slip plane
Segment 2 on dislocation 12	$P = 0.44$	$P = 1.0$
Segment 2 on dislocation 22	$P < 0.01$	$P = 0.63$

Image stresses play an important role in activating the cross-slip by changing the resolved shear stress on the cross-slip planes. For example, when cross-slip occurs, for dislocation 12, the resolved shear stresses resulting from image forces on the cross-slip plane $(1\,1\,\bar{1})$ and on the original plane $(\bar{1}\,1\,1)$ are 37.76 and 20.15 MPa, respectively. The resolved shear stresses resulting from applied stress on the cross-slip plane and the original plane are 46.22 and 48.18 MPa, respectively. The cross-slip plane has even a lower stress without the image effect. The average final resolved shear stresses on the cross-slip plane and the original plane are 81.98 and 60.07 MPa, which shows that surface image forces greatly increase the cross-slip probability on the cross-slip plane. For climb, we calculated the climb stresses on

dislocation 12 and 13 as 208.3 and 294.3 MPa at the end of straining. We believe that these high stresses can lead to pipe diffusion that results in dislocation climb [26,27]. Careful analysis of node coordinates of the simulated and experimental configurations shows great reduction in the positional difference when cross-slip and climb motion are included, with the largest difference for any of the dislocations of about 13 nm in-plane and 17 nm out-of-plane. These uncertainties are well within experimental error.

5. Conclusions

Direct validation of DD simulations with experiments (in situ straining coupled with 3D imaging in TEM) allowed us to correctly model the motion of dislocations in thin, annealed Cu foils with a low initial dislocation density where surface image forces play a significant role in determining the dislocation dynamics. It is shown, through systematic comparison between experimental observations and PDD simulations, that dislocation configurations in thin copper foils acquire considerable 3D components that cannot be explained by glide events alone. The structure of dislocation lines is highly jogged, with non-planar components. Surface image forces in the thin copper foil appear to have two main effects: (1) they result in the inducement of cross-slip for screw components; (2) they also nucleate jogs on dislocation lines. Possibly through vacancy flow from the surface, the motion of these jogs may also result in additional out-of-plane displacement of edge dislocation segments as well.

Acknowledgements

This work at Los Alamos was performed under the auspices of the US Department of Energy (DOE) and was supported by the US DOE, Office of Science, Office of Basic Energy Sciences, Division of Material Sciences. The work at UCLA was supported by the National Science Foundation, Grant No. NSF-DMR-0113555.

References

[1] Tang M, Kubin LP, Canova GR. Acta Mater 1998;46:3221.
[2] Zbib HM, Rhee M, Hirth JP. Int J Mech Sci 1998;40:113.
[3] Schwarz KW. J Appl Phys 1999;85(1):108.
[4] Zbib HM, De la Rubia TD, Rhee M, Hirth JP. J Nucl Mater 2000;276:154.
[5] Ghoniem NM, Sun LZ. Phys Rev B 1999;60:128.
[6] Tong SH, Ghoniem NM, Sun LZ. Phys Rev B 2000;1(1):913.
[7] Ghoniem NM, Huang JM. J Phys IV 2001;11(5):53.
[8] Dehm G, Balk TJ, von Blanckenhagen B, Gumbsch P, Artz E. Zeits Metall 2002;93:383.
[9] Bulatov VV, Tang MJ, Zbib HM. MRS Bull 2001;26:191.
[10] Lagow BW, Robertson IM, Jouiad M, Lassila DH, Lee TC, Birnbaum HK. Mater Sci Engrg A 2001;309:445.
[11] Robertson IM. Engrg Fract Mech 2001;68:671.
[12] Pettinari F, Couret A, Caillard D, Molenat G, Clement N, Coujou A. J Microsc 2001;203:47.
[13] McCabe RJ, Misra A, Mitchell TE. Microsc Microanal 2003;9:29.
[14] Marko M, Leith A. J Struct Biol 1996;116:93.
[15] Bonnevilie J, Escaig B. Acta Metall 1979;27:1477.
[16] Duesbery MS. Model Simul Mater Sci Engrg 1998;6:35.
[17] Zbib HM, Hirth JP, Huang H, Rhee M, de la Rubia MT. Model Simul Mater Sci Engrg 1998;6:467.
[18] Bacon DJ, Hull D. In: Introduction to dislocations. 3rd ed. New York: Pergamon Press; 1984. p. 54.
[19] Indenbom VL, Lothe J, Chamrov VA. Phys Stat Sol (b) 1982;111:671.
[20] Fivel M, Gosling TJ, Canova GR. Model Simul Mater Sci Engrg 1996;4:581.
[21] Kubin LP, Canova G, Condat M, Devincre B, Pontikis V, Bréchet Y. Solid State Phenomena 1992;23–24:455.
[22] Verdier M, Fivel M, Canova GR. Model Simul Mater Sci Engrg 1998;6:755.
[23] Van der Giessen E, Needleman A. Comput Mater Model 1994;42:294.
[24] Martinez R, Ghoniem NM. J Comput Methods Engrg Sci, CMES 2002;3(2):229.
[25] Hirth JP, Lothe J. Theory of dislocations. 2nd ed. New York: McGraw-Hill; 1982.
[26] Turnbull D, Hoffman RE. Acta Metall 1954;2:419.
[27] Love GR. Acta Metall 1964;12:731.